Decoherence rates in complex Josephson qubit circuits

David P. DiVincenzo,[1] Frederico Brito,[2,1] and Roger H. Koch[1]
[1]*IBM T.J. Watson Research Center, P.O. Box 218, Yorktown Heights, New York 10598, USA*
[2]*Departamento de Física da Matéria Condensada, Instituto de Física Gleb Wataghin, Universidade Estadual de Campinas, Campinas-SP 13083-970, Brazil*
(Received 14 November 2005; published 25 July 2006)

A complete analysis of the decoherence properties of a Josephson junction qubit is presented. The qubit is of the flux type and consists of two large loops forming a gradiometer, one small loop, and three Josephson junctions. We develop a complete, quantitative description of the inductances and capacitances of the circuit. Including two stray capacitances makes the quantum mechanical modeling of the system five dimensional. To make the required calculation tractable, we devise a general Born-Oppenheimer approximation which reduces the effective dimensionality in the calculation to one. Contributions to relaxation (T_1) and dephasing (T_ϕ) arising from two different control circuits, one coupled to the small loop and one coupled to a large loop, is computed. We explore T_1 and T_ϕ along an optimal line in the space of applied fluxes; along this "S line" we see significant and rapidly varying contributions to the decoherence parameters, primarily from the circuit coupling to the large loop.

DOI: 10.1103/PhysRevB.74.014514 PACS number(s): 03.67.Lx, 03.65.Yz, 05.30.−d

I. INTRODUCTION

Recent years have seen much success in obtaining high-coherence quantum behavior in a variety of flux-based Josephson-junction qubits. The devices which show good behavior as qubits are fairly complex electrical circuits, and a detailed theoretical analysis of these circuits has proven useful in arriving at optimal designs with the best decoherence behavior.[1,2] Since the first reports of coherent oscillations in Josephson qubits,[3] the observed coherence times have increased by a factor of about 5000; theory has had a substantial role in this large increase (for a theoretical review of Josephson qubits, see Ref. 4), by suggesting strategies for choosing optimal settings of control parameters for the operation of the qubit.

In this paper, we report the results of a detailed theoretical study of the flux qubit recently reported by our group.[5] The paper has two important components. First, we develop a significant extension and simplification of the quantum modeling methodology for Josephson qubits; these theoretical developments are of general applicability and will permit the quantitative analysis of a wide range of complex Josephson circuits. Second, we apply these extensions of the formalism to develop an extensive, detailed set of predictions for the Josephson qubit developed recently at IBM.[6] This second part will explore many details specific to this particular qubit. We believe that these details will be of interest, given the promise that this qubit shows to create a scalable quantum computer.

The methodology that we extend here was introduced by Burkard, Koch, and DiVincenzo (BKD).[7] BKD developed a universal method for analyzing any electrical circuit that can be represented by lumped elements. BKD proceeds in several steps: first, the Kirchhoff equations are formulated in graph theoretic language so that they describe the dynamics of a general circuit in terms of a set of independent, canonical coordinates. Then, one set of terms in these equations of motion (the "lossless" part) is seen to be generated by a Hamiltonian describing a massive particle in a potential; the number of space dimensions in which the particle moves is equal to the number of canonical coordinates in the Kirchhof equations. The "lossy" parts of the equations of motion are treated by introducing a bath of harmonic oscillators, in the style of Caldeira and Leggett.[8]

Section II of the present paper, with the accompanying Appendix, introduces significant improvements to the analysis of BKD.[7] These improvements were necessitated by the fact that we wanted to study the effect of stray capacitances in the qubit circuit of Fig. 1. The quantum mechanics that this model defines is that of a particle in a five-dimensional potential (five because there are three junction capacitances and two stray capacitances, each defining a degree of freedom). A direct, accurate evaluation of the Schrödinger equation in five dimensions is numerically prohibitive. But we find that, in a controlled way, we can organize these five dimensions into four coordinate directions that are "fast" (in which the potential rises very steeply) and one that is "slow" (and has the double-well structure at low Φ_c). Then, just as in molecular physics,[9] the fast coordinates can be treated adiabatically, having the effect of modifying the effective slow potential energy in the one remaining coordinate. The resulting one-dimensional quantum theory is very easy to analyze numerically, and amenable to a qualitative discussion. This idea is developed in generality in Sec. II as a new Born-Oppenheimer approximation. Several accompanying theoretical improvements to Ref. 7 are also developed. A capacitance rescaling, necessary to reliably distinguish fast from slow coordinates, is developed systematically. We also extend the original formalism so that it can treat rapid changes in the external control parameters [Eqs. (A43) and (A44)]. While not important for modeling the IBM experimental work, we expect these formulas to have application to other Josephson qubits.

The second part of this paper, Secs. III–IX apply our formalism to develop detailed predications for the decoherence behavior of the recently reported IBM Josephson qubit.[6] To do this the resulting Hamiltonian obtained theoretically, in-

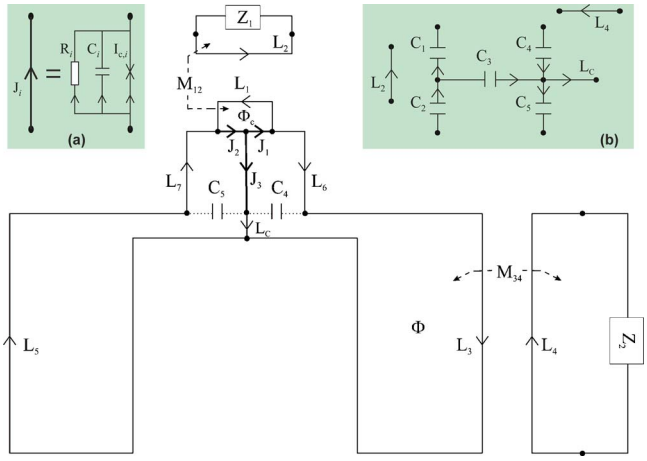

FIG. 1. (Color online) The IBM qubit, drawn as a network graph. This is an oriented graph of the gradiometer structure coupled to two sources Z_1 and Z_2 via mutual inductances M_{12} and M_{34}. Branches of the graph represent Josephson junctions J_i, inductances L_i and external impedances Z_i. Each Josephson junction branch (thick line) is modelled by a resistively shunted Josephson junction (RSJ) containing (a) an ideal junction with critical current $I_{c,i}$, junction capacitance C_i and shunt resistance R_i. C_4 and C_5 denote stray capacitances present in the circuit. The qubit is operated changing the external fluxes Φ_c and Φ applied through the small and large loops, respectively. (b) The tree chosen for the graph. Values used for this qubit: $Lz_i=Z_i(\omega)/i\omega$; $Z_1=Z_2=50\ \Omega$, $I_c=\frac{\Phi_0}{2\pi L_J}=0.8\ \mu A$, $C_i=10$ fF, $C_4=C_5=50$ fF and, using the modeling program FASTHENRY, $L_c=106.27$, $L_1=32.18$, $L_3=L_5=605.03$, $L_6=L_7=81.46$, $L_2=32.18$, $L_4=605.03$, $M_{12}=0.8$, $M_{13}=M_{15}=0.18$, $M_{16}=M_{17}=-2.41$, $M_{3c}=-M_{5c}=0.52$, $M_{34}=0.5$, $M_{35}=3.4$, $M_{36}=M_{57}=0.22$, $M_{37}=M_{56}=-0.86$, $M_{1c}=0$ (exact), $M_{6c}=-M_{7c}=27.63$, $M_{67}=-13.93$ (all in units of pH).

volving a system, a bath, and a system-bath coupling, is analyzed by standard means to determine the decoherence parameters T_1 and T_ϕ of the first two eigenlevels of the system (the "qubit"). T_1 is the energy loss rate of the qubit, while T_ϕ, the "pure dephasing time," is related to the experimental parameter T_2, the decay time of Ramsey fringes, by $T_2^{-1}=\frac{1}{2}T_1^{-1}+T_\phi^{-1}$. Long T_1 and T_ϕ times are both necessary conditions for quantum computing.

The results of this paper have revealed significant facts about the dependence of T_1 and T_ϕ on the control parameters of the IBM qubit. The qubit has, to a good degree of approximation, a bilateral symmetry across its midline (see Fig. 1). This symmetry manifests itself in the quantum behavior. The quantum structure is effectively that of a symmetric double well potential whenever the difference of bias fluxes in the two large loops Φ is the flux quantum $\Phi_0=h/2e$. (The structure is a "gradiometer," meaning that, to good approximation, its behavior is only a function of the difference of the magnetic flux in the two large loops.)

We will analyze the decoherence parameters arising from the two impedances shown, Z_1 and Z_2. Because Z_1 is coupled to the qubit via the "small" loop, we refer to the decoherence parameters associated with it as T_{1s} and $T_{\phi s}$; the corresponding parameters for Z_2, coupled via the "large" loop, are T_{1l} and $T_{\phi l}$. We find that the bilateral symmetry completely controls the overall structure of the T_1's and T_ϕ's. All these parameters are symmetric in Φ around Φ_0 ($T_{\phi l}$ and T_{1l} are approximately symmetric for small values of control flux $\Phi<0.39\Phi_0$, the other two are exactly symmetric). Furthermore, T_{1s}, $T_{\phi s}$, and $T_{\phi l}$ all have divergent behavior at the symmetric point; T_{1s} is exactly divergent, $T_{\phi s}$ and $T_{\phi l}$ are very nearly so for a large range of small-loop control flux Φ_c. These facts give a powerful motivation for operating the qubit always very near $\Phi=\Phi_0$. As a function of Φ_c, $T_{\phi l}$ is strongly increasing and T_{1l} is strongly decreasing (in the symmetric situation). This makes it essential to stay within a particular window of operating parameters.

As we will discuss in detail, the full dependence of the four decoherence parameters on Φ and Φ_c is complex, but can be grossly understood as being controlled by two distinct regimes, the "semiclassical" and the "harmonic." In the semiclassical regime, the effective potential is a double well with a high barrier between, so that quantum tunneling is very small. As Φ_c is increased, the barrier drops, then disappears altogether; then the qubit potential enters the "harmonic" regime, where the potential is approximately just a single, quadratic well. These two extreme cases are relatively simple; decoherence in the regime of crossover between these two is rather complex.

This paper is organized as follows. Section II introduces the network graph formalism that we use to analyze the quantum mechanics of Josephson circuits. We stress the two innovations that considerably streamline the analysis: a capacitance rescaling and a Born-Oppenheimer approximation. The Appendix gives more background about the theory, with subsection 1 giving a review, with some minor corrections, of the relevant parts of BKD,[7] and subsection 2 highlighting some new results in network graph theory. Section III discusses the details of the necessary computation that are specific to the gradiometer qubit. Section IV gives a qualitative discussion of the features of the four decoherence parameters T_{1s}, T_{1l}, $T_{\phi s}$, and $T_{\phi l}$ that we compute. Section V reviews a semiclassical analysis from BKD (Ref. 7) that is helpful in understanding the overall features of the decoherence parameters. Sections VI–IX give an extended discussion of each of the four decoherence parameters. Section X gives some conclusions.

II. ANALYSIS: CAPACITANCE RESCALING AND BORN OPPENHEIMER APPROXIMATION

Our analysis follows closely that of BKD.[7] A summary of the essentials of this theory is given in the Appendix. The result of this theory is, first, a system Hamiltonian, which we begin with here [see Eq. (76)]:

$$\mathcal{H}_S(t)=\frac{1}{2}\mathbf{Q}_C^T\mathbf{C}^{-1}\mathbf{Q}_C+\left(\frac{\Phi_0}{2\pi}\right)^2U(\boldsymbol{\varphi},t), \tag{1}$$

$$U(\varphi,t)=-\sum_i L_{J;i}^{-1}\cos\varphi_i+\frac{1}{2}\boldsymbol{\varphi}^T\mathbf{M}_0\boldsymbol{\varphi}+\frac{2\pi}{\Phi_0}\boldsymbol{\varphi}^T[(\bar{\mathbf{N}}*\boldsymbol{\Phi}_x)(t)+(\bar{\mathbf{S}}*\mathbf{I}_B)(t)]. \tag{2}$$

To perform the Born Oppenheimer approximation, it is best to first go to a rescaled coordinate system in which the mass (i.e., the capacitance matrix $\mathbf{C}$) is isotropic. This is mentioned in BKD,[7] but we present this analysis more generally here to set our notation. We make the following coordinate transformation:

$$\mathbf{q} = c^{1/2}\mathbf{C}^{-1/2}\mathbf{Q}_C, \tag{3}$$

$$\mathbf{f} = c^{-1/2}\mathbf{C}^{1/2}\boldsymbol{\varphi}, \tag{4}$$

c is some standard capacitance; it is convenient to insert this arbitrary number so that q and f have the same units as Q_C and φ, respectively. Note that the commutation relations are left unchanged by this coordinate change

$$\frac{\Phi_0}{2\pi}(\varphi_i Q_{C,j} - Q_{C,j}\varphi_i) = i\hbar\,\delta_{ij} \rightarrow \frac{\Phi_0}{2\pi}(f_i q_j - q_j f_i) = i\hbar\,\delta_{ij}. \tag{5}$$

The Hamiltonian for the rescaled Schrödinger equation is

$$\mathcal{H}_S(t) = \frac{1}{2c}\mathbf{q}^T\mathbf{q} + \left(\frac{\Phi_0}{2\pi}\right)U'(\mathbf{f},t), \tag{6}$$

$$U'(\mathbf{f},t) = -\sum_i L_{J;i}^{-1}\cos[c^{1/2}(\mathbf{C}^{-1/2}\mathbf{f})_i] + \frac{1}{2}\mathbf{f}^T(c\mathbf{C}^{-1/2}\mathbf{M}_0\mathbf{C}^{-1/2})\mathbf{f} + \frac{2\pi}{\Phi_0}\mathbf{f}^T[c^{1/2}\mathbf{C}^{-1/2}(\bar{\mathbf{N}} * \boldsymbol{\Phi}_x)(t) + c^{1/2}\mathbf{C}^{-1/2}(\bar{\mathbf{S}} * \mathbf{I}_B)(t)]. \tag{7}$$

For computing decoherence parameters, we take over unchanged the golden rule formulas discussed in BKD (Ref. 7) (see Appendix):

$$\frac{1}{T_1} = 4|\langle 0|\mathbf{m}\cdot\boldsymbol{\varphi}|1\rangle|^2 J(\omega_{01})\coth\frac{\omega_{01}}{2k_BT}, \tag{8}$$

$$\frac{1}{T_\phi} = |\langle 0|\mathbf{m}\cdot\boldsymbol{\varphi}|0\rangle - \langle 1|\mathbf{m}\cdot\boldsymbol{\varphi}|1\rangle|^2 \left.\frac{J(\omega)}{\omega}\right|_{\omega\to 0} 2k_BT. \tag{9}$$

For the rescaled coordinates, these are

$$\frac{1}{T_1} = 4|\langle 0|c^{1/2}\mathbf{m}^T\mathbf{C}^{-1/2}\mathbf{f}|1\rangle|^2 J(\omega_{01})\coth\frac{\omega_{01}}{2k_BT}, \tag{10}$$

$$\frac{1}{T_\phi} = |\langle 0|c^{1/2}\mathbf{m}^T\mathbf{C}^{-1/2}\mathbf{f}|0\rangle - \langle 1|c^{1/2}\mathbf{m}^T\mathbf{C}^{-1/2}\mathbf{f}|1\rangle|^2 \left.\frac{J(\omega)}{\omega}\right|_{\omega\to 0} 2k_BT. \tag{11}$$

Recall that there is a different T_1 and T_ϕ for each external impedance Z_i (ignoring nonadditivity[10]); the circuit-theoretic vector $\mathbf{m}$ in these formulas [Eqs. (A21) and (A41)] determines how much the quantum noise from Z_i couples to each of the Josephson phases $\boldsymbol{\varphi}$.

We will discuss the use of the Born-Oppenheimer approximation to evaluate these formulas. What must be computed are matrix elements of the form

$$\int d\mathbf{f}(\mathbf{v}\cdot\mathbf{f})\langle\alpha|\mathbf{f}\rangle\langle\mathbf{f}|\beta\rangle, \tag{12}$$

where $\alpha,\beta = 0,1$, and $\mathbf{v}$ is the constant vector $c^{1/2}\mathbf{m}^T\mathbf{C}^{-1/2}$.

As discussed in the introduction, we single out one (more than one is also possible) "slow" degree of freedom $\mathrm{f}_\parallel$, and take all coordinate directions orthogonal to this one $\mathbf{f}_\perp$ to be "fast." So

$$\mathbf{f} = \{\mathrm{f}_\parallel, \mathbf{f}_\perp\}. \tag{13}$$

The fast coordinates are characterized by the fact that the potential $U'(\mathbf{f})$ increases very rapidly in the $\mathbf{f}_\perp$ direction; we assume that it is a good approximation to expand in these directions to second order

$$U'(\mathbf{f}) \approx V(\mathrm{f}_\parallel) + \sum a_i(\mathrm{f}_\parallel)\mathbf{f}_{\perp,i} + \sum b_{ij}(\mathrm{f}_\parallel)\mathbf{f}_{\perp,i}\mathbf{f}_{\perp,j}, \tag{14}$$

where $\mathbf{b}$ can be taken to be a real symmetric matrix.

In this case, the Born-Oppenheimer approximation is made as follows:[9] fix the slow coordinate $\mathrm{f}_\parallel$, solve the remaining (harmonic) Schrödinger equation in fast coordinates $\mathbf{f}_\perp$. The ground state eigenvalue of this Schrödinger equation is

$$u(\mathrm{f}_\parallel) = \left(\frac{\Phi_0}{2\pi}\right)^2 V(\mathrm{f}_\parallel) - \left(\frac{\Phi_0}{2\pi}\right)^2\frac{1}{4}\mathbf{a}^T\mathbf{b}^{-1}\mathbf{a} + \frac{\hbar}{\sqrt{2c}}\mathrm{Tr}\sqrt{\mathbf{b}}. \tag{15}$$

Note that this effective potential has nontrivial $\mathrm{f}_\parallel$ dependence from its last two terms. The first and second terms represent the value of the potential (in the $\mathbf{f}_\perp$ coordinates), and the final term is the sum of the zero point energies $\frac{1}{2}\hbar\omega$ in this multidimensional harmonic well.

The minimum of the potential in the $\mathbf{f}_\perp$ coordinates, as a function of $\mathrm{f}_\parallel$, is

$$\mathbf{f}_\perp^{\min}(\mathrm{f}_\parallel) = -\frac{1}{2}\mathbf{b}^{-1}(\mathrm{f}_\parallel)\mathbf{a}(\mathrm{f}_\parallel). \tag{16}$$

The ground state wavefunction in the $\mathbf{f}_\perp$ coordinates is a gaussian centered at this point, which we will indicate as

$$\langle\mathbf{f}_\perp|0,\mathrm{f}_\parallel\rangle = g[\mathbf{f}_\perp - \mathbf{f}_\perp^{\min}(\mathrm{f}_\parallel)]. \tag{17}$$

In the Born-Oppenheimer approximation, the full wave function is taken to be

$$\langle\mathbf{f}|\alpha\rangle = \langle\mathrm{f}_\parallel|\alpha\rangle\langle\mathbf{f}_\perp|0,\mathrm{f}_\parallel\rangle = \langle\mathrm{f}_\parallel|\alpha\rangle g[\mathbf{f}_\perp - \mathbf{f}_\perp^{\min}(\mathrm{f}_\parallel)]. \tag{18}$$

Where $\langle\mathrm{f}_\parallel|\alpha\rangle$ is the αth eigenstate of the one-dimensional, slow-coordinate Schrödinger equation

$$\left[-\left(\frac{2\pi}{\Phi_0}\right)^2\frac{\hbar^2}{2c}\frac{d^2}{d\mathrm{f}_\parallel^2} + u(\mathrm{f}_\parallel)\right]\langle\mathrm{f}_\parallel|\alpha\rangle = \lambda_\alpha\langle\mathrm{f}_\parallel|\alpha\rangle. \tag{19}$$

We return to the matrix elements that are to be computed, Eq. (12). We separate the integrand into a fast and a slow part:

$$\int d\mathbf{f}(\mathbf{v}\cdot\mathbf{f})\langle\alpha|\mathbf{f}\rangle\langle\mathbf{f}|\beta\rangle = \int d\mathbf{f}(\mathbf{v}_\perp\cdot\mathbf{f}_\perp + \mathbf{v}_\parallel \mathrm{f}_\parallel)\langle\alpha|\mathbf{f}\rangle\langle\mathbf{f}|\beta\rangle = \int d\mathrm{f}_\parallel d\mathbf{f}_\perp \mathbf{v}_\perp\cdot\mathbf{f}_\perp\langle\alpha|\mathrm{f}_\parallel\rangle\langle\mathrm{f}_\parallel|\beta\rangle g^2[\mathbf{f}_\perp - \mathbf{f}_\perp^{\min}(\mathrm{f}_\parallel)] + \int d\mathrm{f}_\parallel d\mathbf{f}_\perp \mathbf{v}_\parallel \mathrm{f}_\parallel\langle\alpha|\mathrm{f}_\parallel\rangle$$
$$\times\langle\mathrm{f}_\parallel|\beta\rangle g^2[\mathbf{f}_\perp - \mathbf{f}_\perp^{\min}(\mathrm{f}_\parallel)] = \int d\mathrm{f}_\parallel\langle\alpha|\mathrm{f}_\parallel\rangle\langle\mathrm{f}_\parallel|\beta\rangle \int d\mathbf{f}_\perp \mathbf{v}_\perp\cdot\mathbf{f}_\perp g^2[\mathbf{f}_\perp - \mathbf{f}_\perp^{\min}(\mathrm{f}_\parallel)] + \int d\mathrm{f}_\parallel \mathbf{v}_\parallel \mathrm{f}_\parallel\langle\alpha|\mathrm{f}_\parallel\rangle$$
$$\times\langle\mathrm{f}_\parallel|\beta\rangle \int d\mathbf{f}_\perp g^2[\mathbf{f}_\perp - \mathbf{f}_\perp^{\min}(\mathrm{f}_\parallel)] = \int d\mathrm{f}_\parallel[\mathbf{v}_\perp\cdot\mathbf{f}_\perp^{\min}(\mathrm{f}_\parallel)]\langle\alpha|\mathrm{f}_\parallel\rangle\langle\mathrm{f}_\parallel|\beta\rangle + \int d\mathrm{f}_\parallel \mathbf{v}_\parallel \mathrm{f}_\parallel\langle\alpha|\mathrm{f}_\parallel\rangle\langle\mathrm{f}_\parallel|\beta\rangle. \quad (20)$$

In the last line we use the fact that the Gaussian is a normalized transverse wave function. The final two-term expression of Eq. (20) will be used below in the evaluation of the T_1 and T_ϕ expressions. The Schrödinger equation solutions [Eq. (19)] and all the necessary integrations are performed numerically in MATHEMATICA.

III. RESULTS FOR THE GRADIOMETER QUBIT

We have calculated the coherence properties of the gradiometer qubit of Koch *et al.*,[5] assuming coupling to two different lossy circuits, one inductively coupled to the small loop, and the other inductively coupled to one of the large loops (see Fig. 1). Here we do not include the additional structure considered in Ref. 5, a low-loss terminated transmission line inductively coupled to the other large loop (not shown). This structure strongly modifies the quantum behavior of the qubit when the energy splitting of the ground and first excited state of the qubit is large (comparable to 1.5 GHz, a typical resonant frequency for the terminated transmission line); however, for smaller energy gaps this structure is expected to be unimportant. The two lossy structures included are expected to account for most of the dissipative and decohering processes seen by the qubit.

It is known that the decohering effect of two such structures is nonadditive, see Brito and Burkard (Ref. 10); but they show that this nonadditive effect is typically small, and we will consider the irreversible effects of each structure separately. We have extended the analysis of Ref. 5 to include the effect of stray capacitances on the qubit quantum behavior. We approximate the distributed stray capacitances as two new lumped circuit elements, shown with dotted lines in Fig. 1. Including these capacitors, the circuit theory leads to a quantum description of the qubit that is equivalent to that of a particle in a five-dimensional potential. Using the Born-Oppenheimer analysis developed in this paper, the complexity of the calculation is not too greatly increased by these additional capacitances. As we will see, these extra capacitances, even though their capacitances are larger than the junction capacitances, cause only quantitative differences in the behavior of the decoherence parameters.

Figure 2 shows a two-dimensional slice of the potential U', after rescaling the capacitance matrix as indicated in Eqs. (3) and (4). The slice is chosen to include the two eigendirections of the rescaled curvature matrix of the quadratic part of the U' potential [$\mathbf{C}^{-1/2}\mathbf{M}_0\mathbf{C}^{-1/2}$ of Eq. (7)]. In one of these directions the curvature is zero; in this direction only the Josephson energy is nonzero, and the potential is periodic (about two periods are shown in the figure). This periodicity reflects the 2π periodicity of the superconducting phase of the central island of the circuit (the place where J1, J2, and J3 meet in Fig. 1). The displacement of the two-dimensional plane shown in Fig. 2 is chosen so that the inductive energy is minimized—recall that the inductive energy consists of a quadratic and a linear part.

The two dots in Fig. 2 indicate the minimum energy points of the potential in this plane, which is almost (but not precisely) the position of the absolute minima (these have also a small component in the other three coordinate directions). We choose the "slow" coordinate $\mathrm{f}_\parallel$ of the Born-Oppenheimer approximation to be along the line connecting the two minima in the plane shown; the other four directions are treated as the "fast coordinates."

Figure 3 gives more detail about the potential in these "fast" directions. As expected, the potential rises more

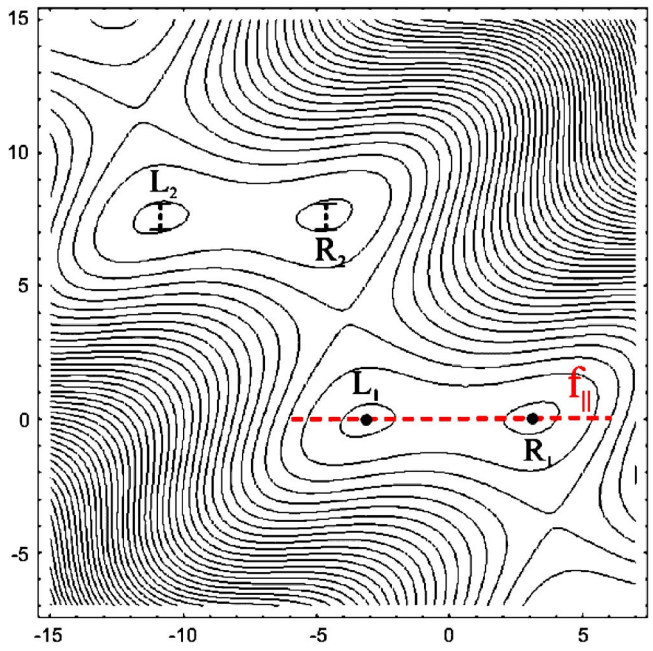

FIG. 2. (Color online) Contour plot of the potential $U'(\mathbf{f})$ on the S line for the external fluxes $\Phi_c=0.36\Phi_0$ and $\Phi=\Phi_0$. The red dashed line indicates the "slow" direction $\mathrm{f}_\parallel$. Along this direction the potential is a symmetric double well, with the two relevant minima of the potential indicated by dots. The bars show the spatial extension of the wave function, in the vicinity of the minima, in the "fast" direction $\mathrm{f}_\perp$ with the smallest curvature of the potential.

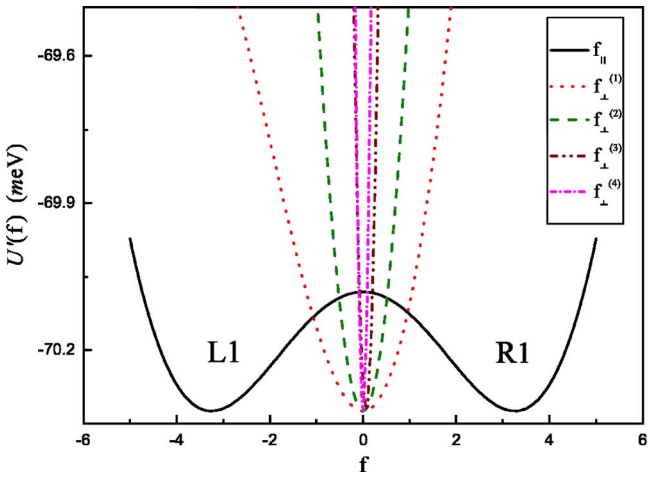

FIG. 3. (Color online) Plots of the potential U', in the vicinity of the relevant minima, for each one of the orthogonal components of **f**. These plots were done by keeping fixed four coordinates at their minimum points and varying the other one. For the "slow" direction $f_{\|}$ (solid line) we see a double well structure (symmetric on S line). Along the "fast" coordinates $f_{\perp}^{(i)}$, here calculated at the L1 point, a an almost harmonic well is present. The external fluxes used for these plots were $\Phi_c=0.36\Phi_0$ and $\Phi=\Phi_0$.

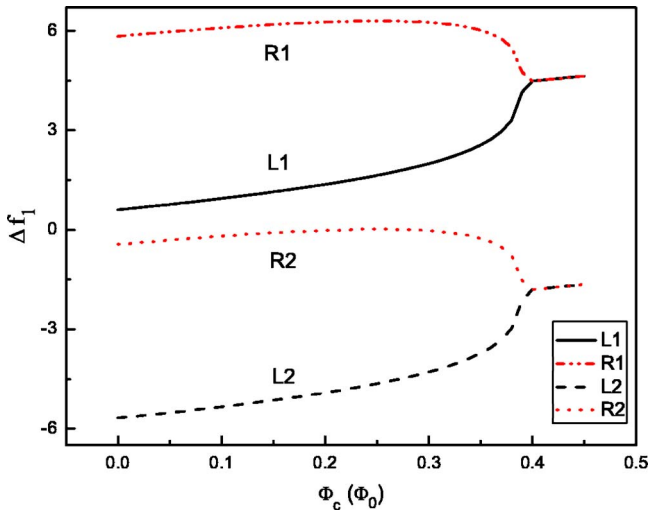

FIG. 4. (Color online) The values of the phase associated with the Josephson junction J_1 at the minima of the potential, as function of the "control" flux Φ_c, along the S line. Two consecutive pairs of minima (L_i-R_i) along the periodic direction are shown. Near $\Phi_c \gtrsim 0.39$, the double-minimum structure collapses rapidly to a single minimum per period; in this regime the distance between the single minima $(i)-(i+1)$ is 2π.

steeply in all these directions than in the "slow" direction. The potentials are all basically harmonic, with some noticeable anharmonicity, particularly in the softest "fast" direction $f_{\perp}^{(1)}$. But a calculation of the extent of the ground wave function in this direction (error bars near L2 and R2 in Fig. 2) shows that it remains well confined within the harmonic region.

We have chosen a "symmetric" setting for the parameters $\Phi=\Phi_0$ such that the potential is a symmetric double well—the depth of the pair of potential minima in Fig. 2 is equal. This defines a line in the Φ-Φ_c plane that we refer to as the "S line" (S for symmetric). As the external control parameters Φ and Φ_c are varied, this potential landscape is changed in two different ways.

(1) As Φ_c is varied, the distance between the two minima, and thus the height of the barrier separating them, varies. Increasing Φ_c from the value shown, $\Phi_c=0.36\Phi_0$, the distance between L1 and R1 (L and R for "left" and "right") drops rapidly, as shown by Figs. 4–8, which show how these minimum points evolve as a function of Φ_c along the S line. As the minima approach one another, the height of the barrier separating the L1 and R1 minima decreases rapidly, as shown in Fig. 9. In this regime the quantum-mechanical tunnel splitting between the lowest-lying energy levels increases dramatically, see Fig. 10. Around $\Phi_c=0.39\Phi_0$ the barrier vanishes entirely. There follows a long interval of Φ_c in which there is only a single minimum per period of the potential; when Φ_c increases a little beyond $\Phi_c=0.39\Phi_0$, the potential becones quite harmonic around its minimum.

(2) As Φ is varied around Φ_0, the energies of the two minima are shifted with respect to one another. For larger excursions of Φ away from Φ_0, one minimum becomes unstable, and only one minimum per period remains stable.

Figure 11 shows a large region of the Φ-Φ_c plane, simulating a sequence of measurements very much as they are done in the experiment: For a sequence of values of Φ_c, Φ is scanned from left to right and back again. Each scan (nearly hoizontal line) plots the value of Φ_c, plus a signal proportional to the classical circulating current in one of the large loops of the qubit. The most prominent feature of this sequence of curves is the thin vertical regions in which the scans are hysteretic. This essentially plots the region in which there is a double minimum in the potential. The shape of this region reflects the behavior of the barrier height with

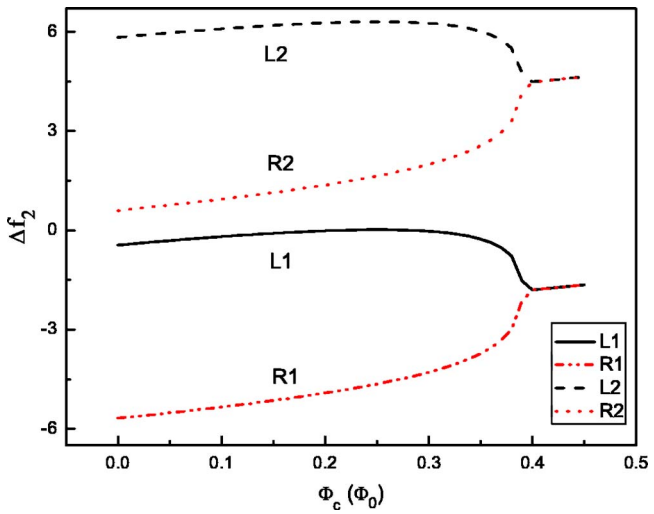

FIG. 5. (Color online) The values of the phase associated with the Josephson junction J_2 at the minima of the potential, as function of the "control" flux Φ_c, along the S line. Two consecutive pairs of minima (L_i-R_i) along the periodic direction are shown. Near $\Phi_c \gtrsim 0.39$, the double-minimum structure collapses rapidly to a single minimum per period; in this regime the distance between the single minima $(i)-(i+1)$ is 2π.

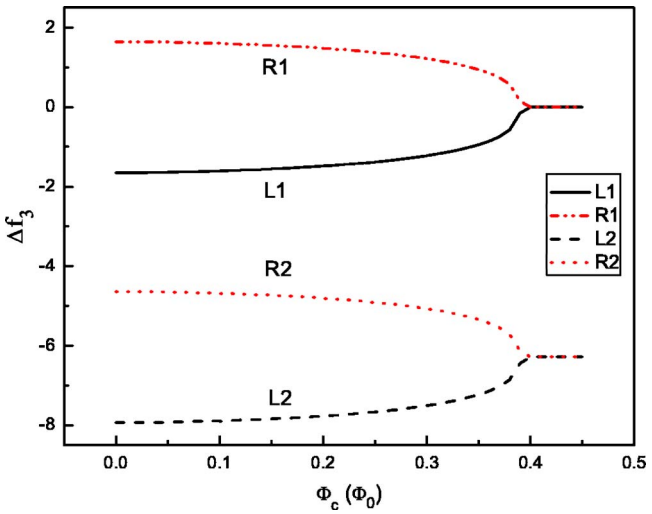

FIG. 6. (Color online) The values of the phase associated with the Josephson junction J_3 at the minima of the potential, as function of the "control" flux Φ_c, along the S line. Two consecutive pairs of minima (L_i-R_i) along the periodic direction are shown. Near $\Phi_c \gtrsim 0.39$, the double-minimum structure collapses rapidly to a single minimum per period; in this regime the distance between the single minima $(i)-(i+1)$ is 2π.

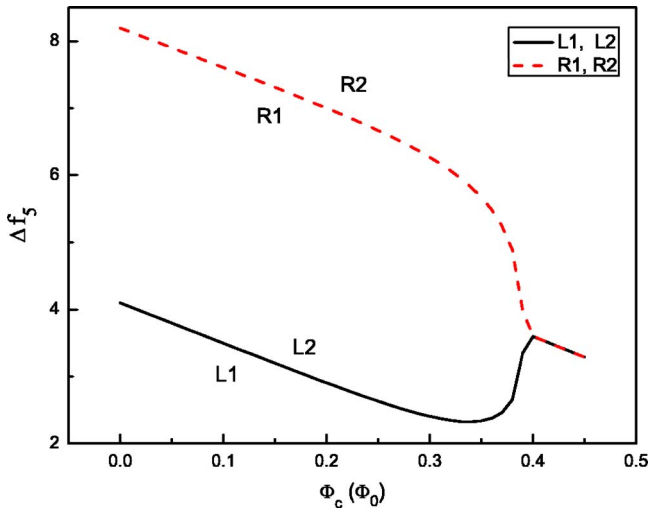

FIG. 8. (Color online) The values of the phase associated with the stray capacitance C_5 at the minima of the potential, as function of the "control" flux Φ_c, along the S line. (The phase of a capacitance is proportional to the time integral of the voltage across the capacitor.) For this phase all minima pairs (L_i-R_i) with the same values. This occurs because of the *absence* of a Josephson energy term dependent on this phase.

control flux, Fig. 9. Looking at flux $\Phi=\Phi_0$, one sees, as one decreases the control flux Φ_c from about $0.4\Phi_0$, a rapid widening of the hysteresis feature, reflecting a rapid increase of the barrier height. The abrupt switch to shrinkage of the hysteresis loop reflects a switching of the lowest barrier from the L1-R1 line to the L1-R2 line. This cuspy feature is readily seen in the experiment,[6] and is an excellent landmark for calibrating the actual applied fluxes.

Figure 11 is clearly periodic with changes in applied flux. Since Φ and Φ_c are Aharonov-Bohm fluxes (i.e., involving no magnetic field penetrating the interior of the conductors), changing either by an integer multiple of Φ_0 should leave the quantum behavior of the system invariant. This is actually *not* the periodicity that is seen in Fig. 11. This absence of Aharonov-Bohm periodicity, an apparent violation of gauge invariance, is a result of the fact that the outer perimeter of the qubit is not interrupted by a Josephson junction; because the temperature is very low compared with the superconducting energy gap, there is a very high barrier to the motion of a flux quantum into or out of the device. If this barrier is

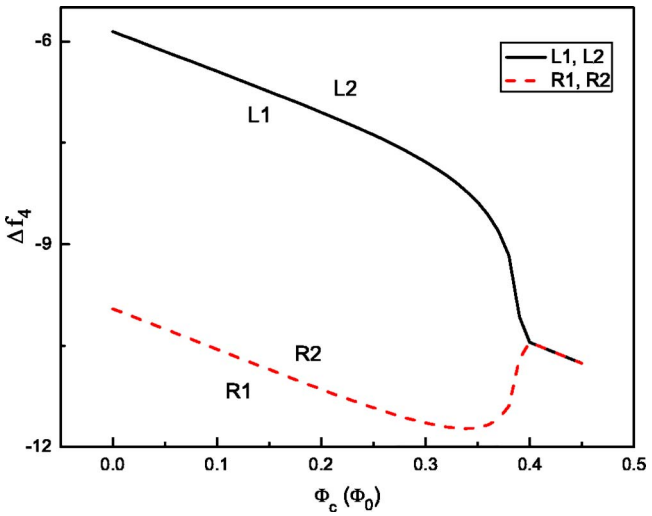

FIG. 7. (Color online) The values of the phase associated with the stray capacitance C_4 at the minima of the potential, as function of the "control" flux Φ_c, along the S line. (The phase of a capacitance is proportional to the time integral of the voltage across the capacitor.) For this phase all minima pairs $(Li-Ri)$ with the same values. This occurs because of the *absence* of a Josephson energy term dependent on this phase.

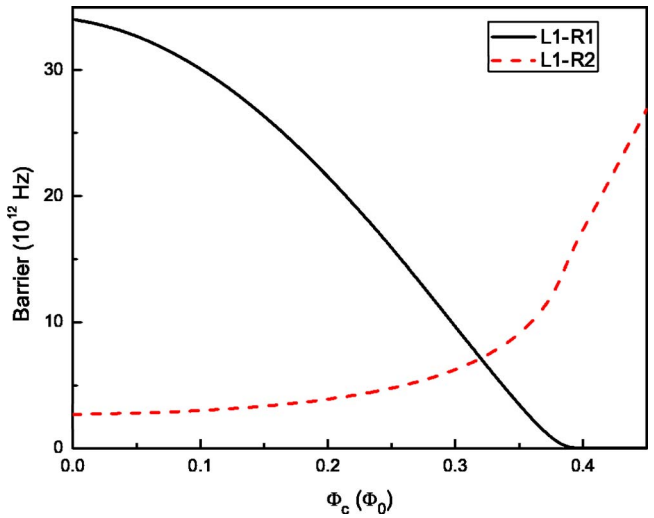

FIG. 9. (Color online) The value of the potential barrier on the S line as a function of Φ_c. Both the L1-L2 barrier height (solid black) and the L1-L2 barrier height (dashed red) are shown. The height of the barrier separating the L1-R1 decreases rapidly as these minima approach one another. For $\Phi_c \gtrsim 0.39$, the barrier vanishes entirely between L1 and R1.

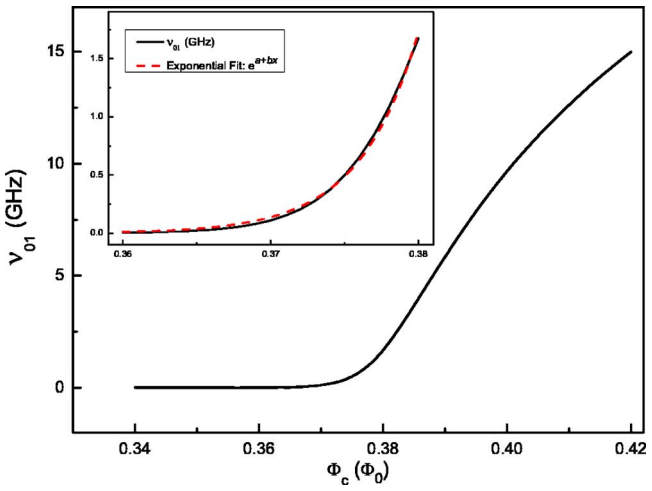

FIG. 10. (Color online) The energy difference between the ground and first eigenstate, $h\nu_{01}=\langle 1|\mathcal{H}_S|1\rangle-\langle 0|\mathcal{H}_S|0\rangle$, as a function of the "control" flux Φ_c on S line. Inset: Detailed view. The red dashed line represents a exponential fit of the data, giving a reasonable representation of the data in this vicinity.

assumed to be infinite (as it effectively is in our model), the states of the device fall into noncommunicating sectors.

Within these sectors, there remains the periodicity with respect to varying the external fluxes seen in the figure: we can show that if Φ is changed by an integer multiple of Φ_0 $(k_1-k_2-2k_3)\Phi_0$ (each k_i is any integer), the qubit Hamiltonian is invariant if Φ_c is simultaneously changed by $-(k_1+k_2)-\frac{L_1}{L_3+L_6}(k_2+k_3)$. This shift of Φ and Φ_c are associated with the phase changes $\Delta f_1=2\pi k_1$, $\Delta f_2=2\pi k_2$, $\Delta f_3=2\pi k_3$, $\Delta f_4=\frac{2\pi}{\sqrt{c}}\left[-k_1+k_3+\frac{L_6}{L_3+L_6}(k_2+k_3)\right]$ and $\Delta f_5=-\frac{2\pi}{\sqrt{c}}\frac{L_3}{L_3+L_6}(k_2+k_3)$. The inductance factors in these expressions are approximate: they are only true in the limit that all mutual inductances are zero. The pattern of invariance as described by these equations is closely matched in experimental data.

The construction of the quadratic and linear parts of the potential in Eq. (7) require a graph-theoretic analysis of the

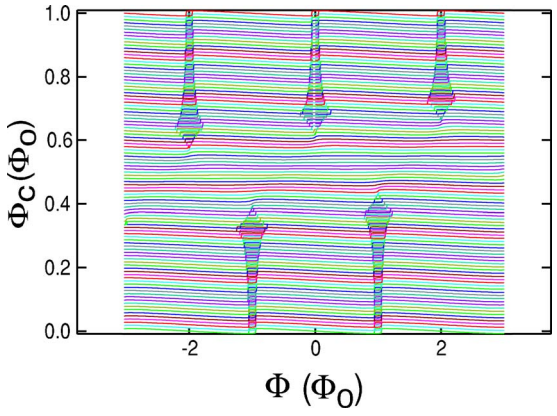

FIG. 11. (Color online) Simulated scans of the critical current over a wide region of the $\Phi-\Phi_c$ plane. These scans periodically show hysteresis in vertically oriented regions in this plane, indicating the presence of the double minimum of the potential in these regions.

gradiometer circuit, Fig. 1. An appropriate tree for the circuit graph is shown in the inset (b) of Fig. 1. Using this, the loop matrices defined in the Appendix, Eq. (A2), can be read off by inspection:

$$F_{CL}=\begin{pmatrix}-1&0&0&-1&0\\-1&0&0&0&-1\\0&0&0&1&-1\\0&1&0&-1&0\\0&0&1&0&-1\end{pmatrix},\quad F_{CZ}=\begin{pmatrix}0&0\\0&0\\0&0\\0&0\\0&0\end{pmatrix}, \tag{21}$$

$$F_{KL}=\begin{pmatrix}0&0&0&0&0\\0&0&0&0&0\\0&1&-1&0&0\end{pmatrix},\quad F_{KZ}=\begin{pmatrix}-1&0\\0&-1\\0&0\end{pmatrix}. \tag{22}$$

For the numerical analysis of decoherence parameters, we need values for the physical parameters of the circuit. For the **C** matrix, circuit modeling indicates that we can take it to be a diagonal matrix with diagonal elements {10, 10, 10, 50, 50} (in units of fF). The 10 fF capacitances are for the Josephson junctions, the 50 fF capacitances are the "strays." Although the strays are numerically the largest capacitances, they do not affect the results qualitatively, because of their positions in the circuit.

The **L** matrices are denoted

$$L=\begin{pmatrix}L_1&M_{13}&M_{15}&M_{16}&M_{17}\\M_{13}&L_3&M_{35}&M_{36}&M_{37}\\M_{15}&M_{35}&L_3&M_{56}&M_{57}\\M_{16}&M_{36}&M_{56}&L_6&M_{67}\\M_{17}&M_{37}&M_{57}&M_{67}&L_6\end{pmatrix},$$

$$L_{LK}=\begin{pmatrix}M_{12}&0&M_{1c}\\0&M_{34}&M_{3c}\\0&0&M_{5c}\\0&0&M_{6c}\\0&0&M_{7c}\end{pmatrix}, \tag{23}$$

$$L_K=\begin{pmatrix}L_2&0&0\\0&L_4&0\\0&0&L_c\end{pmatrix},\quad L_Z=\begin{pmatrix}Lz_1&0\\0&Lz_2\end{pmatrix}. \tag{24}$$

The numerical values of these parameters are given in the caption of Fig. 1.

The decoherence parameters involve the temperature, which we take as $T=5$ K. This rather high temperature, much larger than the bath temperature of a dilution refrigerator, is an accurateempirical value for the effective noise temperature of the circuits coupled to the qubit. Future experiments are planned which will make this effective temperature much lower.

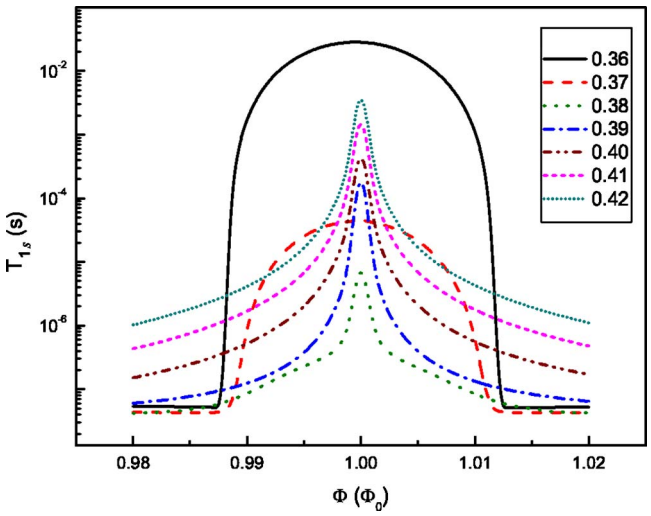

FIG. 12. (Color online) The relaxation time T_{1s} associated with the dissipation source Z_1. The T_{1s} plots are presented as a function of changes in the small- and large-loop fluxes, Φ_c and Φ, respectively. As a consequence of a high potential barrier, up to $\Phi_c \approx 0.39$ the data can be well described by a semiclassical model, see Eq. (36). For $\Phi_c \gtrsim 0.39\Phi_0$, the behavior is nearly that in a harmonic potential. The mathematical symmetry seen around $\Phi=\Phi_0$ occurs because of the bilateral symmetry of the qubit. The break around $\delta=\pm 0.01$ $[\Phi=(1+\delta)\Phi_0]$ indicates that for larger δ the lowest two eigenstates are both located in one well.

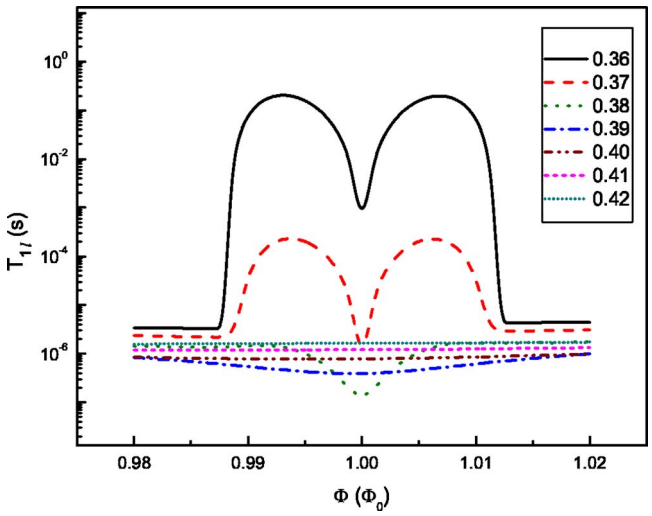

FIG. 13. (Color online) The relaxation time T_{1l} associated with the dissipation source Z_2. The T_{1l} plots are presented as a function of changes in the small- and large-loop fluxes Φ_c and Φ, respectively. As with T_{1s}, T_{1l} has two distinct regions, the "semiclassical" ($\Phi_c \lesssim 0.39\Phi_0$) and the "harmonic" ($\Phi_c \gtrsim 0.39\Phi_0$). The approximate symmetry around $\Phi=\Phi_0$ arises from the dominant $\|$ contributions to the matrix element (30).

The formal applied flux vector is $\Phi_{\mathbf{x}}=\{\Phi_{\mathbf{c}},\Phi,\Phi_{\mathbf{p}},0,0\}$. Φ_c and Φ have been introduced previously, and Φ_p is the flux in the third loop, the "pick up loop." Φ_p will always to be taken to be zero in the analyses here.

With these matrices we compute the coefficients $\mathbf{M}_0$ and $\bar{\mathbf{N}}(\omega)$ using the formulas in the Appendix [Eqs. (A17) and (A18)] [$\bar{\mathbf{S}}(\omega)$ does not occur, as no current sources are present in the circuit]. The applied fluxes are time dependent in the experiments that we are modeling, so in principle we need to retain the full frequency dependence of $\bar{\mathbf{N}}(\omega)$. The presence of a frequency dependence in this operator is indicative of a retardation phenomenon: the Hamiltonian at time t is *not* a function only of the applied fluxes at time t; rather, because of the lossy elements in the circuit, $H(t)$ depends on a convolution of Φ_x over times preceding t. We find, however, that the range in time of the kernel $\bar{\mathbf{N}}(t)$ in this convolution is very short: this time range is set by $L_2/\mathrm{Re}[Z_1(\omega=0)]$ and $L_4/\mathrm{Re}[Z_2(\omega=0)]$. For our parameters, this time is no more that 10 ps. In experiments,[5] the applied fluxes are varied on a time scale greater than 100 ps. For this reason, we ignore this retardation effect in all our calculations here, and set $\bar{\mathbf{N}}(\omega)=\bar{\mathbf{N}}(\omega=0)$.

IV. DISCUSSION OF T_1 AND T_ϕ

Figures 12–15 show the obtained dissipation and decoherence rates obtained for the gradiometer qubit in the vicinity of the symmetric line, shown as a function of changes in the small- and large-loop bias fluxes (Φ_p is taken to be zero throughout). The dependences of these quantities is complex, with variations over a large range of values (note that all the plots are logarithmic). We can explain all the trends seen in these curves. Several key facts determine the overall structure of these curves.

Many of the curves have a break around $\Phi=(1\pm\delta)\Phi_0$, $\delta\approx 0.01$. This is a consequence of a level crossing that occurs near this value of δ: for larger $|\delta|$ the lowest two energy eigenvalues of the qubit are both in one energy well. Thus,

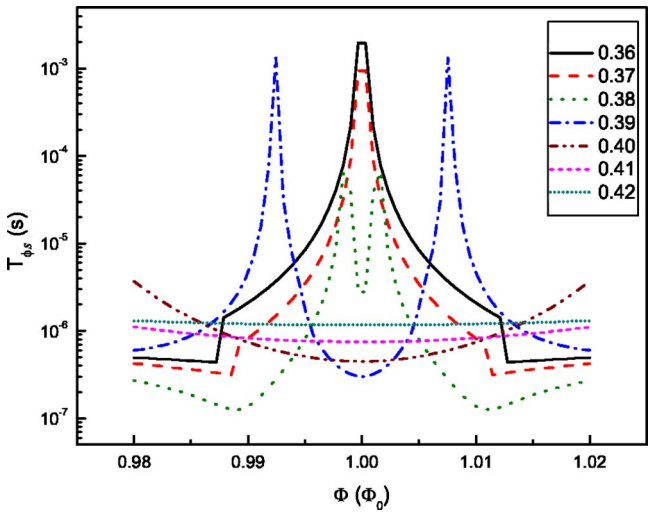

FIG. 14. (Color online) The dephasing time associated with the dissipation source Z_1. The $T_{\phi s}$ plots are presented as a function of changes in the small- and large-loop fluxes Φ_c and Φ, respectively. The two-peak structure is understood as a manifestation of nonequal weight of the states $|0\rangle$ and $|1\rangle$ in the matrix elements Eq. (31). The mathematical symmetry seen around $\Phi=\Phi_0$ occurs because of the bilateral symmetry of the qubit.

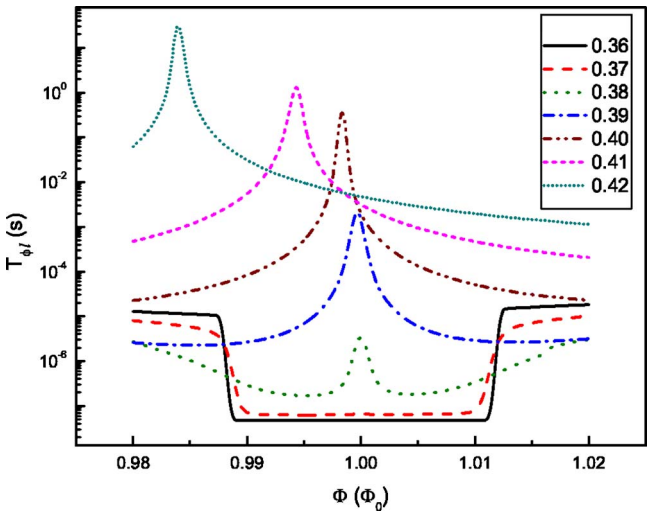

FIG. 15. (Color online) The dephasing time associated with the dissipation source Z_2. The $T_{\phi l}$ plots are presented as a function of changes in the small- and large-loop fluxes Φ_c and Φ, respectively. The significant breaking of symmetry around the S line occurs due the transverse contributions to the matrix elements Eq. (31), and is associated with the unsymmetrical way that this source couples to the qubit.

for $|\delta| > 0.01$ the system is too unsymmetrical for the two qubit states to correspond to the left and right wells, and consequently the results in this regime are not of great interest to us.

For small values of the control flux $\Phi_c \lesssim 0.39\Phi_0$ the barrier is high, and the wave function weight is concentrated near the minima of the two wells. In this regime, which was referred to as the "semiclassical" regime in BKD, the various curves vary in predictable ways as the barrier height and well asymmetry are changed, as we will detail shortly.

For large values of the control flux $\Phi_c \gtrsim 0.39\Phi_0$ the barrier vanishes, and the single remaining well rapidly becomes almost exactly harmonic. It is straightforward to calculate what happens to T_1 and T_ϕ in this harmonic limit, and we will see that the data in this regime can be understood with reference to this limit.

The lossy circuit coupled to the small loop respects the bilateral symmetry of the gradiometer qubit. An exact consequence of this is that T_{1s} and $T_{\phi s}$ are mathematically symmetric around $\Phi = \Phi_0$.

The lossy circuit coupled to the large loop does *not* respect the bilateral symmetry of the qubit. Consequently, T_{1l} and $T_{\phi l}$ are not symmetric, but for several separate reasons (different ones in the semiclassical and harmonic regimes) these functions, for the most part, are very nearly symmetric. Actually, if the Born-Oppenheimer corrections to the decoherence parameters, derived in Sec. II, were left out, T_{1l} would be exactly symmetric.

The s curves (T_{1s} and $T_{\phi s}$) are very different from the l curves (T_{1l} and $T_{\phi l}$). This perhaps surprising result is explained by the fact that the s functions have exactly no contribution from the longitudinal term in the matrix elements [first term in Eq. (20)]. The longitudinal term usually dominates the transverse term [second term in Eq. (20)] when it is present, as it is for the l functions. As we will see, this makes the character of these curves very different from one another.

V. REVIEW OF SEMICLASSICAL ANALYSIS

As in BKD, we assume that the potential $U'(\mathbf{f})$ describes a double well with "left" and "right" minima at

$$\mathbf{f}_L = \{\mathrm{f}_{\|L}, \mathbf{f}_\perp^{\min}(\mathrm{f}_{\|L})\}, \tag{25}$$

$$\mathbf{f}_R = \{\mathrm{f}_{\|R}, \mathbf{f}_\perp^{\min}(\mathrm{f}_{\|R})\}. \tag{26}$$

Then, the semiclassical approximation amounts to assuming that the left and right single-well ground states $|L\rangle$ and $|R\rangle$ centered at $\mathbf{f}_{L,R}$ are localized orbitals, having amplitude that vanishes very rapidly away from these minima. Then the two lowest eigenstates can approximately be written as the symmetric and antisymmetric combinations of $|R\rangle$ and $|L\rangle$,

$$|0\rangle = \frac{1}{\sqrt{2}}\left(\sqrt{1+\frac{\epsilon}{\omega_{01}}}|L\rangle + \sqrt{1-\frac{\epsilon}{\omega_{01}}}|R\rangle\right), \tag{27}$$

$$|1\rangle = \frac{1}{\sqrt{2}}\left(\sqrt{1-\frac{\epsilon}{\omega_{01}}}|L\rangle - \sqrt{1+\frac{\epsilon}{\omega_{01}}}|R\rangle\right), \tag{28}$$

where $\omega_{01} = \sqrt{\Delta^2+\epsilon^2}$, $\epsilon = \langle L|\mathcal{H}_S|L\rangle - \langle R|\mathcal{H}_S|R\rangle$ is the asymmetry of the double well, and $\Delta = \langle L|\mathcal{H}_S|R\rangle$ is the tunneling amplitude between the two wells. Δ increases almost exponentially with Φ_c as expected in a WKB picture, see Fig. 10. Since $|L\rangle$ and $|R\rangle$ are localized orbitals, we approximate the matrix elements [see Eq. (20)]:

$$\langle L|\mathbf{v}\cdot\mathbf{f}|R\rangle \approx 0, \quad \langle L|\mathbf{v}\cdot\mathbf{f}|L\rangle \approx \mathbf{v}\cdot\mathbf{f}_L, \quad \langle R|\mathbf{v}\cdot\mathbf{f}|R\rangle \approx \mathbf{v}\cdot\mathbf{f}_R. \tag{29}$$

From Eqs. (27)–(29) the eigenstate matrix elements are

$$\langle 0|\mathbf{v}\cdot\mathbf{f}|1\rangle \approx \frac{1}{2}\frac{\Delta}{\omega_{01}}\mathbf{v}\cdot\Delta\mathbf{f}, \tag{30}$$

$$\langle 0|\mathbf{v}\cdot\mathbf{f}|0\rangle - \langle 1|\mathbf{v}\cdot\mathbf{f}|1\rangle \approx \frac{\epsilon}{\omega_{01}}\mathbf{v}\cdot\Delta\mathbf{f}, \tag{31}$$

where $\Delta\mathbf{f} = \mathbf{f}_L - \mathbf{f}_R$. These formulas will be applied in different ways to explain the four quantities in Figs. 12–15.

In this semiclassical approximation with localized states, the relaxation and decoherence times both diverge if $\Delta\mathbf{f}$ can be made orthogonal to $\mathbf{v}$. For a symmetric double well ($\epsilon = 0$), $T_\phi \to \infty$ for all $\Delta\mathbf{f}$.

VI. T_{1s}

We see in Fig. 12 that as Φ_c increases, T_{1s} initially is almost constant in ϵ and decreasing exponentially with Φ_c; this behavior changes fairly abruptly to one which is exponentially *increasing* in Φ_c, with a sharp maximum at $\epsilon = 0$. The initial behavior is explained by the semiclassical theory. We must specialize the semiclassical theory to a fact that is special to the circuit coupling to the small loop: as a consequence of the bilateral symmetry of the structure, the "naive"

longitudinal contribution to the matrix elements vanishes, i.e.,

$$\mathbf{v}_{\parallel} = 0. \tag{32}$$

With this, we can specialize the T_1 matrix element Eq. (30) thus

$$|\langle 0|\mathbf{v}\cdot\mathbf{f}|1\rangle|^2 \approx \frac{1}{4}\frac{\Delta^2}{\omega_{01}^2}\{\mathbf{v}_{\perp}\cdot[\mathbf{f}_{\perp}(f_{\parallel}^L) - \mathbf{f}_{\perp}(f_{\parallel}^R)]\}^2. \tag{33}$$

We find that, again as a consequence of symmetry, the function $\mathbf{f}_{\perp}(f_{\parallel})$ has a special form: at the symmetric-well point, it is an even function of $f_{\parallel}$ (assuming the origin is centered at the midpoint between the two wells); in addition, this symmetry is broken continuously as ϵ is made nonzero. This can be summarized by writing the start of the Taylor series for $\mathbf{v}\cdot\mathbf{f}_{\perp}(f_{\parallel})$:

$$\mathbf{v}\cdot\mathbf{f}_{\perp}(f_{\parallel}) = af_{\parallel}^2 + b\epsilon f_{\parallel} + \cdots . \tag{34}$$

Plugging this in and using $f_{\parallel}^R = -f_{\parallel}^L$ for $\epsilon = 0$ gives

$$|\langle 0|\mathbf{v}\cdot\mathbf{f}|1\rangle|^2 \approx \frac{1}{4}\frac{\Delta^2}{\omega_{01}^2} \times b^2\epsilon^2(f_{\parallel}^R)^2, \tag{35}$$

$$T_{1s} \propto \frac{\omega_{01}^2}{\Delta^2\epsilon^2} = \frac{1}{\Delta^2} + \frac{1}{\epsilon^2}. \tag{36}$$

This simple functional form fits the curves in Fig. 12 very well for $\Phi_c = 0.36 - 0.39\Phi_0$.

For larger Φ_c the trend of T_{1s} is explained by the observation that around $\Phi_c = 0.39\Phi_0$, the barrier disappears and the single minimum rapidly approaches being an ideal harmonic potential. If the potential were exactly harmonic, with its minimum-curvature direction pointed in the $\parallel$ direction, then T_1 would diverge. The exponential growth of T_{1s} in this regime reflects this approach to harmonicity. At all values of Φ_c it remains true that for $\Phi = \Phi_0$, T_{1s} is divergent, and the lineshapes around $\Phi = \Phi_0$ reflect this.

VII. T_{1l}

T_{1l} also has two distinct regions, the "semiclassical" and the "harmonic." In both regions, the longitudinal contributions to the matrix element dominate. This means that symmetry-breaking contributions [for $\Phi = (1 \pm \delta)\Phi_0$] remain very small in all regimes (this is untrue for $T_{\phi l}$).

The semiclassical prediction for T_{1l} is

$$T_{1l}^{-1} \propto |\langle 0|\mathbf{v}\cdot\mathbf{f}|1\rangle|^2 \approx \frac{1}{4}\frac{\Delta^2}{\omega_{01}^2}[\mathbf{v}_{\parallel}(f_{\parallel}^L - f_{\parallel}^R)]^2. \tag{37}$$

Since $f_{\parallel}^{L,R}$ is slowly varying with Φ and Φ_c, we have

$$T_{1l} \propto 1 + \frac{\epsilon^2}{\Delta^2}. \tag{38}$$

This equation predicts a T_{1l} which is exponentially decreasing overall, with a deep minimum at $\Phi = \Phi_0$, as seen in the figure.

When the potential becomes harmonic, then T_{1l} should approach a constant almost independent of Φ, since the harmonic oscillator wavefunctions are only shifted by the force proportional to $\Phi - \Phi_0$; the matrix element is independent of this force. T_{1l} is seen to slowly vary with Φ_c: the variation that is seen presumably reflects the small increase in the harmonic frequency as Φ_c increases.

VIII. $T_{\phi s}$

The semiclassical approximation follows the same development as for T_{1s}, with the result [see Eq. (35)]

$$|\langle 0|\mathbf{v}\cdot\mathbf{f}|0\rangle - \langle 1|\mathbf{v}\cdot\mathbf{f}|1\rangle|^2 \approx \frac{\epsilon^2}{\omega_{01}^2} \times b^2\epsilon^2(f_{\parallel}^R)^2, \tag{39}$$

$$T_{\phi s} \propto \frac{\omega_{01}^2}{\epsilon^4} = \frac{1}{\epsilon^2} + \frac{\Delta^2}{\epsilon^4}. \tag{40}$$

This last equation predicts a strongly diverging $T_{\phi s}$ with not very much Δ (i.e., Φ_c) dependence, as is seen initially in Fig. 14.

There is a fairly rapid departure from the semiclassical prediction for $T_{\phi s}$ in that the divergence at $\Phi = \Phi_0$ splits (symmetrically, as discussed above) into two which rapidly move away from the center. This is explained by the fact that, once the wave functions become somewhat delocalized, the difference between the 0 and 1 matrix elements in Eq. (39) becomes nonzero, pushing the divergence away from the symmetric point. This difference becomes nonzero because the 0 state (the symmetric state at $\Phi = \Phi_0$) has more amplitude between the two minima than the 1 (antisymmetric) state. Thus, when weighted by the $\mathbf{v}\cdot\mathbf{f}_{\perp}(f_{\parallel})$ function [recall Eq. (34)], the 0 and 1 matrix elements are (initially) slightly different.

In the harmonic limit, $T_{\phi s}$ should diverge, just as T_{1s} does. Comparing Figs. 12–14 though, shows that the details of this divergence are rather different. It is evident that as this limit is approached, $T_{\phi l}$ is dominated by the remaining differences of the 0 and 1 matrix elements just discussed, which become nearly Φ independent as the 0 and 1 wave functions become more harmonic.

IX. $T_{\phi l}$

$T_{\phi l}$ is shown in Fig. 15. In the semiclassical regime this should be

$$T_{\phi l}^{-1} \propto |\langle 0|\mathbf{v}\cdot\mathbf{f}|0\rangle - \langle 1|\mathbf{v}\cdot\mathbf{f}|1\rangle|^2 \approx \frac{\epsilon^2}{\omega_{01}^2}[\mathbf{v}_{\parallel}(f_{\parallel}^L - f_{\parallel}^R)]^2. \tag{41}$$

So

$$T_{\phi l} \propto \frac{\epsilon^2 + \Delta^2}{\epsilon^2}. \tag{42}$$

For small Δ this predicts, as seen, an almost Φ_c-independent behavior, with a very weak divergence at $\Phi = \Phi_0$. As Δ increases, the divergence gets stronger and $T_{\phi l}$ begins to increase overall.

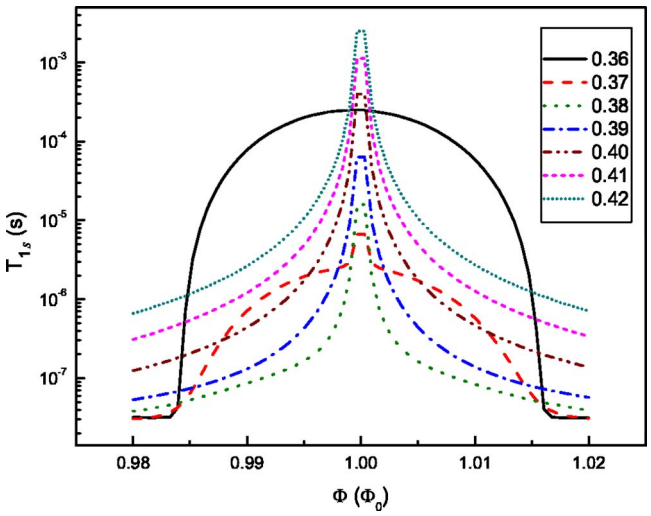

FIG. 16. (Color online) T_{1s} for the case without stray capacitances ($C_4=C_5=0$). We see the same qualitative behavior compared with that observed in Fig. 12.

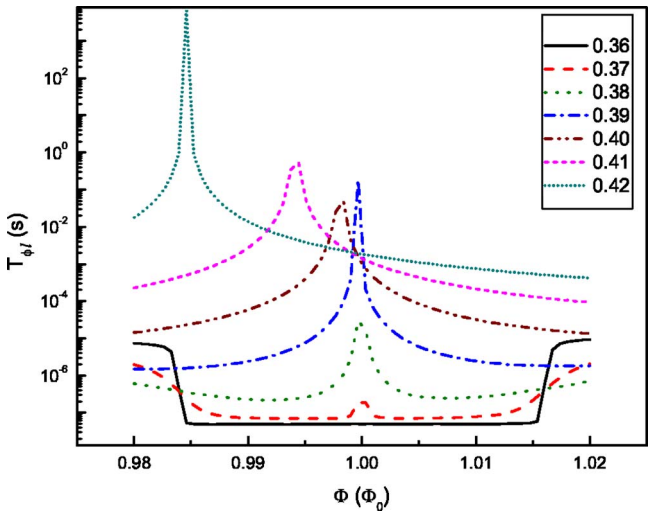

FIG. 17. (Color online) $T_{\phi l}$ for the case without stray capacitances ($C_4=C_5=0$). We see the same qualitative behavior as that observed in Fig. 14.

In the harmonic limit, again, $T_{\phi l}$ should diverge. But as the $\|$ contributions disappear, eventually the transverse contributions to the matrix elements begin to be important. These explicitly break the symmetry, as can easily be seen as the shifting of the divergence point in the last few $T_{\phi l}$ curves.

However, this asymmetry is unlikely to be noticeable experimentally. Recall that the physical T_ϕ and T_1 are (approximately[10]) given by summing the s and l rates. The strong asymmetry in $T_{\phi l}$ occurs only when its contribution to the rate is very small, and the symmetric $T_{\phi s}$ will dominate.

X. DISCUSSION AND CONCLUSIONS

We conclude with a discussion of the effect of the presence of stray capacitances, and on the overall implication of our results on decoherence parameters for experiments on the gradiometer qubit. Figures 16 and 17 show the results for T_{1s} and $T_{\phi l}$ for the gradiometer qubit with zero assumed stray capacitances. Graphically, the results are apparently only slightly changed. This is somewhat an impression created by the log scale; a closer examination of the T_1 result shows that the presence of stray capacitances actually *improves* the relaxation time (i.e., makes it longer) by about a factor of 10 in the double-well region, while leaving it more or less unchanged in the harmonic, single-well region.

Figures 18 and 19 provide some explanation for this observation. We see that the double-well potential profile is very similar in the two cases, with the well depths being virtually the same. However, the presence of the strays pushes apart the rescaled distance between the two minima. This diminishes the tunneling between the two wells, and, not surprisingly therefore, lengthens the relaxation time to go from one well to the other. In Fig. 19 we see that this effect persists right up to the point where the two minima merge at around $\Phi_c=0.39\Phi_0$.

Finally, Fig. 20 gives perhaps the most experimentally relevant summary of our results for the realistic gradiometer qubit parameters (with stray capacitances). During qubit operation, it is envisioned[5] that the qubit will be initialized at small control flux, and will then be pulsed rapidly up to high control flux; above $\Phi_c=0.38-0.39\Phi_0$, we expect the coherence of the qubit to be protected by an oscillator stabilization not discussed here.

The preferred initialization point is at a value of Φ_c well below $0.36\Phi_0$. We see that here we have the right conditions for initialization of the qubit, in that the T_1 time will be very long—the figure shows it increasing exponentially as Φ_c is

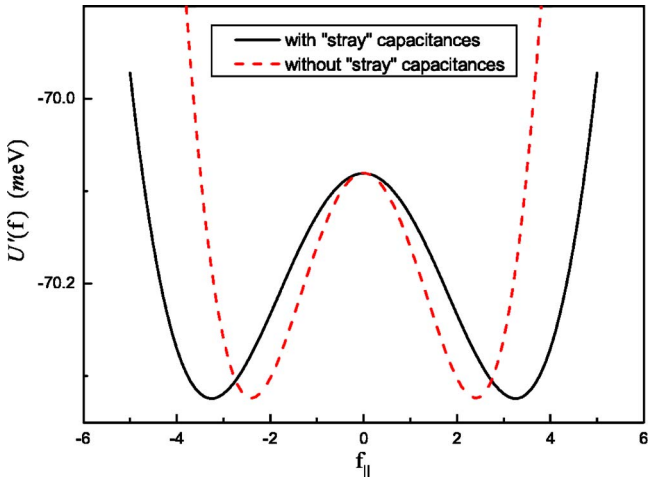

FIG. 18. (Color online) Potential $U'(\mathbf{f})$, Eq. (7), along the "slow" coordinate $f_\|$ for the cases with (black solid line) and without (red dashed line) stray capacitances. The same effective capacitance c is used for both. It is observed that the height of barrier is almost the same for both cases (the difference is less than $10^{-6}\%$) while the distance between the minima changes appreciably. Because of these facts one might expect that the tunnelling rate should be higher for the case without "stray" capacitances, and thus the T_1 should be shorter. This is seen in our calculations—compare Figs. 13 and 16. The external fluxes used for these plots are $\Phi_c=0.36\Phi_0$ and $\Phi=\Phi_0$.

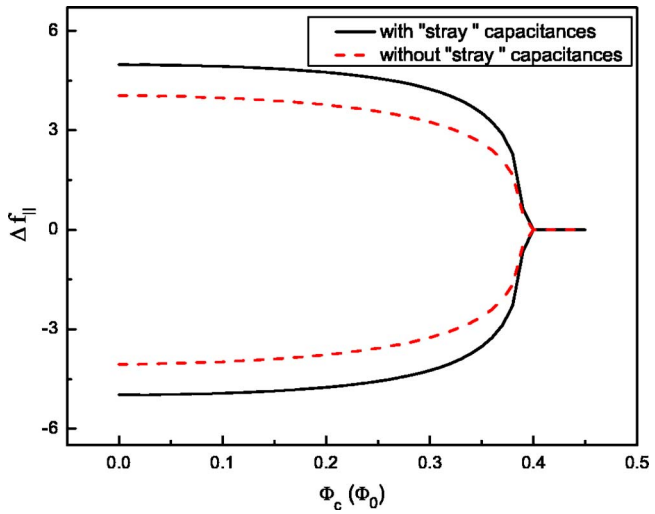

FIG. 19. (Color online) The "slow" coordinate $f_{\|}$ minima, for the relevant minima ($L_i - R_i$), as a function of Φ_c along the S line. We compare the evolution for the cases with (black solid line) and without (red dashed line) stray capacitances.

decreased. This is a simple reflection of the very large barrier height in this region. T_ϕ, and therefore T_2 are very small in this region, but this is not harmful during initialization. When Φ_c is pulsed upwards, quantum dynamics turn on in a region around $\Phi_c = 0.36 - 0.37\Phi_0$, where the 0–1 frequency is increasing exponentially through the 100 MHz range. This is the relevant frequency because it is roughly the inverse of the anticipated rise time of the pulse in this region, 1–10 ns; this is referred to as the "portal" region in Ref. 5.

Thus, the crucial region for the operation of the qubit is in the range of $\Phi_c = 0.37 - 0.38\Phi_0$. It is evidently a very perilous region for the qubit: T_1 is plunging downward, dropping to around 200 ns, and T_2 is increasing from its very small values in the initialization region, but does not rise far beyond 100 ns in this region. Since we expect[5] to pulse through this region in under 10 ns, these times are acceptable for qubit operation; but we see that the qubit could not function if it were held in this region of Φ_c without any other protective mechanism for a long time. Also, we must beware of other effects, such as higher effective temperatures or stronger mutual inductance couplings, that would make these times even worse. We believe that there have been occasions when the conditions of the experiment were worse by a factor of 10 or more; in this case, the qubit's coherence is not likely to survive even a 10 ns traversal of this region of parameter space.

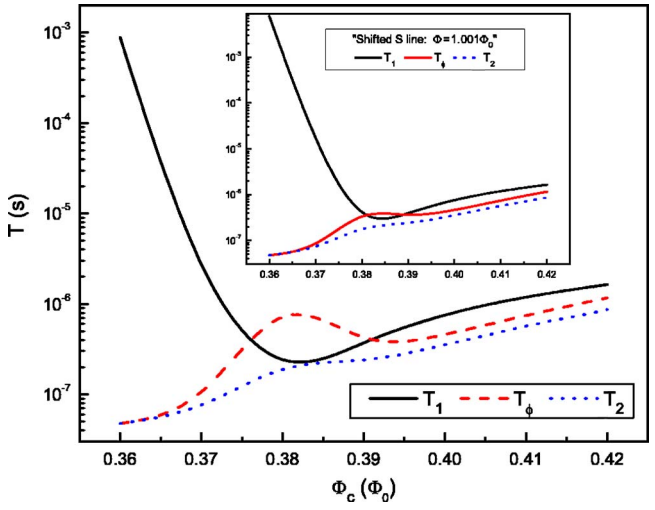

FIG. 20. (Color online) The total relaxation, dephasing and decoherence times (T_1, T_ϕ, and T_2, respectively) along the S line. We can see that T_ϕ (T_1) strongly increases (decreases) as a function of Φ_c. These facts cause there to be a window of desirable operating parameters for the qubit. Inset: Illustrating that the behavior of these times when the flux Φ is shifted by 0.1% away from the S line.

Figure 20 is obtained by adding the inverse relation times arising from the small-loop and large-loop circuits (we ignore the small nonadditive effects explored in Ref. 10). T_1 is, though the whole region of interest, dominated by T_{1l}. For small Φ_c, T_ϕ is also dominated by the large-loop circuit; however, for $\Phi_c > 0.38\Phi_0$ the small-loop dephasing becomes dominant. So, we see that the analysis of both circuits is experimentally relevant.

Finally, the inset to Fig. 20 shows the effects of imperfections in the setting of Φ, which would put the system off the S line. We see that, even for departures of $1m\Phi_0$, there are noticeable changes in the decoherence parameters. T_1 is actually increased, reflecting the fact that T_{1l} has a minimum at the S line. But the system's sensitivity to phase fluctuations increases $-T_\phi$ is smaller off the S line. While the changes seen $1m\Phi_0$ from the S line are not dramatic, these results indicate that much larger departures should be treated with caution, and subject to a full analysis.

A concluding word. The results reported here have been a useful guide to experiment, but they have shown their greatest worth when they are part of the iterative design process itself. Thus, even the rather complete snapshot given here does not do justice to the full role that this analysis has had in the process of perfecting the gradiometer qubit. The work has already passed on to further questions not touched on here, such as the role of additional harmonic oscillator circuits in modifying the decoherence parameters,[5,6] and the problems created by introducing qubit-qubit coupling. An intimate relationship between theory and experiment will continue to be crucial in the continuing development of this qubit technology.

ACKNOWLEDGMENTS

D.P.D.V. is supported in part by the NSA and ARDA through ARO Contract No. W911NF-04-C-0098. F.B. is supported by Fundação de Amparo à Pesquisa do Estado de São Paulo (FAPESP). R.H.K. thanks the support of DARPA under Contract No. MDA972-01-C-0052.

APPENDIX: CIRCUIT THEORY

We make extensive use here of the systematic analysis of flux qubits initiated in BKD. For completeness, we review the formalism presented there, both the network graph theory and the Caldeira-Leggett analysis. We have added some ex-

tensions to this theory, which we separate out and present in a separate subsection of this appendix.

Review of BKD

This subsection is a streamlined summary of the results presented in Ref. 7. An oriented graph $\mathcal{G}=(\mathcal{N},\mathcal{B})$ consists of N nodes $\mathcal{N}=\{n_1,\ldots,n_N\}$ and B branches $\mathcal{B}=\{b_1,\ldots,b_B\}$. In circuit analysis, a branch $b_i=(n_{a(i)},n_{b(i)})$ represents a two-terminal element (resistor, capacitor, inductor, current, or voltage source, etc.), connecting its beginning node $n_{a(i)}$ to its ending node $n_{b(i)}$. A loop in $\mathcal{G}$ is a connected subgraph of $\mathcal{G}$ in which all nodes have degree two (the degree of a node $n\in\mathcal{N}$ is the number of branches containing n). For each connected subgraph we choose a tree $\mathcal{T}_i$, i.e., a connected subgraph of $\mathcal{G}_i$ which contains all its nodes and has no loops. The branches that do not belong to the tree are called "chords." The fundamental loops $\mathcal{F}_i$ of a subgraph $\mathcal{G}_i$ are defined as the set of loops in $\mathcal{G}_i$ which contain exactly one chord $f_i\in\mathcal{G}_i\backslash\mathcal{T}_i$.

A complete description of the topology of the network is provided by the fundamental loop matrix, defined as

$$\mathbf{F}_{ij}^{(L)}=\begin{cases}1, & \text{if } b_j\in\mathcal{F}_i \text{ (same direction as } f_i),\\ -1, & \text{if } b_j\in\mathcal{F}_i \text{ (direction opposite to } f_i),\\ 0, & \text{if } b_j\in\mathcal{F}_i,\end{cases} \tag{A1}$$

where $i=1,\ldots,F$ and $j=1,\ldots,B$. By labeling the branches of the graph $\mathcal{G}$ such that the first $N-P$ branches belong to the tree $\mathcal{T}$, where P is the number of disjoint connected subgraphs of $\mathcal{G}$, we obtain

$$\mathbf{F}^{(L)}=(-\mathbf{F}^T|\mathbb{1}), \tag{A2}$$

where $\mathbf{F}$, the loop matrix, is an $(N-P)\times(B-N+P)$ matrix.

The state of an electric circuit described by a network graph can be defined by the branch currents $\mathbf{I}=(I_1,\ldots,I_B)$, where I_i denotes the electric current flowing in branch b_i, and the branch voltages $\mathbf{V}=(V_1,\ldots,V_B)$, where V_i denotes the voltage drop across the branch b_i. If we divide the branch currents and voltages into a tree and a chord part

$$\mathbf{I}=(\mathbf{I}_{\mathrm{tr}},\mathbf{I}_{\mathrm{ch}}), \tag{A3}$$

$$\mathbf{V}=(\mathbf{V}_{\mathrm{tr}},\mathbf{V}_{\mathrm{ch}}). \tag{A4}$$

Then the Kirchhoff laws can be stated very succinctly and universally:

$$\mathbf{F}\mathbf{I}_{\mathrm{ch}}=-\mathbf{I}_{\mathrm{tr}}, \tag{A5}$$

$$\mathbf{F}^T\mathbf{V}_{\mathrm{tr}}=\mathbf{V}_{\mathrm{ch}}-\dot{\mathbf{\Phi}}_x. \tag{A6}$$

Here Φ_x are the external magnetic fluxes threading the loops.

To write the Hamiltonian of the electrical circuit, we must further distinguish the different types of electrical circuit elements in the graph. We write

$$\mathbf{F}=\begin{pmatrix}\mathbf{F}_{CJ} & \mathbf{F}_{CL} & \mathbf{F}_{CR} & \mathbf{F}_{CZ} & \mathbf{F}_{CB}\\ \mathbf{F}_{KJ} & \mathbf{F}_{KL} & \mathbf{F}_{KR} & \mathbf{F}_{KZ} & \mathbf{F}_{KB}\end{pmatrix}. \tag{A7}$$

The submatrices $\mathbf{F}_{XY}$ will be called loop sub matrices. The different chord labels are for Josephson junctions (J), linear inductors (L), shunt resistors (R), and other external impedances (Z), and bias current sources (B). Without loss of generality the capacitors (C) can all be taken as tree branches. The tree inductors are labeled (K). We note here that in our formalism all capacitors should be considered to be in parallel with a Josephson junction, even if it is one with zero critical current.

Finally, to fully define the problem, the electrical characteristics of each branch type should be defined. The current-voltage relations for the various types of branches are

$$\mathbf{I}_J=\mathbf{I}_{\mathbf{c}}\sin\boldsymbol{\varphi}, \tag{A8}$$

$$\mathbf{Q}_C=\mathbf{C}\mathbf{V}_C, \tag{A9}$$

$$\mathbf{V}_R=\mathbf{R}\mathbf{I}_R, \tag{A10}$$

$$\mathbf{V}_Z(\omega)=\mathbf{Z}(\omega)\mathbf{I}_Z(\omega), \tag{A11}$$

$$\begin{pmatrix}\mathbf{\Phi}_L\\ \mathbf{\Phi}_K\end{pmatrix}=\begin{pmatrix}\mathbf{L} & \mathbf{L}_{LK}\\ \mathbf{L}_{LK}^T & \mathbf{L}_K\end{pmatrix}\begin{pmatrix}\mathbf{I}_L\\ \mathbf{I}_K\end{pmatrix}. \tag{A12}$$

Here the diagonal matrix $\mathbf{I}_{\mathrm{c}}$ contains the critical currents $I_{\mathrm{c},i}$ of the junctions on its diagonal, and $\sin\boldsymbol{\varphi}$ is the vector $(\sin\varphi_1,\sin\varphi_2,\ldots,\sin\varphi_{N_J})$. Equation (A9) describes the (linear) capacitors ($\mathbf{C}$ is the capacitance matrix), and the junction shunt resistors are described by Eq. (A10), where R is the (diagonal and real) shunt resistance matrix. The external impedances are described by the relation Eq. (A11) between the Fourier transforms of the current and voltage, where $\mathbf{Z}(\omega)$ is the impedance matrix. The external impedances can also defined in the time domain

$$\mathbf{V}_Z(t)=\int_{-\infty}^{t}\mathbf{Z}(t-\tau)\mathbf{I}_Z(\tau)d\tau\equiv(\mathbf{Z}*\mathbf{I}_Z)(t), \tag{A13}$$

where the convolution is defined as

$$(\mathbf{f}*\mathbf{g})(t)=\int_{-\infty}^{t}\mathbf{f}(t-\tau)\mathbf{g}(\tau)d\tau. \tag{A14}$$

Causality allows the response function to be nonzero only for positive times, $\mathbf{Z}(t)=0$ for $t<0$. In frequency space, the replacement $\omega\to\omega+i\epsilon$ with $\epsilon>0$ guarantees convergence of the Fourier transform[11]

$$\mathbf{Z}(\omega)=\int_{-\infty}^{\infty}\mathbf{Z}(t)e^{i\omega t}\,dt=\int_{0}^{\infty}\mathbf{Z}(t)e^{i\omega t}\,dt. \tag{A15}$$

In our formalism it is necessary to distinguish chord from tree inductors, so the inductance matrix must be written in block form shown in Eq. (A12).

With all these definitions, a universal equation of motion for the electric circuit reads

$$\mathbf{C}\ddot{\boldsymbol{\varphi}}=-\mathbf{L}_J^{-1}\sin\boldsymbol{\varphi}-\mathbf{M}_0\boldsymbol{\varphi}-\frac{2\pi}{\Phi_0}(\bar{\mathbf{N}}*\mathbf{\Phi}_x)(t)-\frac{2\pi}{\Phi_0}(\bar{\mathbf{S}}*\mathbf{I}_B)(t)-\mathbf{R}^{-1}\dot{\boldsymbol{\varphi}}-\mathbf{M}_d*\boldsymbol{\varphi}. \tag{A16}$$

This equation as presented is a slight extension of BKD, in that $\mathbf{\Phi}_x$ and $\mathbf{I}_B$ are allowed to be time dependent. If they are time independent, then the expressions for the coefficients of this equation of motion are

$$\mathbf{M}_0 = \bar{\mathbf{N}}(\omega=0)\mathbf{F}_{CL}^T, \tag{A17}$$

$$\bar{\mathbf{N}}(\omega=0) = \mathbf{F}_{CL}\tilde{\mathbf{L}}_L^{-1}\bar{\mathbf{L}}\mathbf{L}_{LL}^{-1}. \tag{A18}$$

$$\mathbf{M}_d(\omega) = \bar{\mathbf{m}}\bar{\mathbf{L}}_Z(\omega)^{-1}\bar{\mathbf{m}}^T, \tag{A19}$$

$$\bar{\mathbf{S}}(\omega=0) = \mathbf{F}_{CB} - \mathbf{F}_{CL}(\mathbf{L}_{LL}^{-1})^T\bar{\mathbf{F}}_{KL}^T\tilde{\mathbf{L}}_K^T\mathbf{F}_{KB}, \tag{A20}$$

$$\bar{\mathbf{m}} = \mathbf{F}_{CZ} - \mathbf{F}_{CL}(\mathbf{L}_{LL}^{-1})^T\bar{\mathbf{F}}_{KL}^T\tilde{\mathbf{L}}_K^T\mathbf{F}_{KZ}. \tag{A21}$$

With the definitions, as given in Ref. 7

$$\bar{\mathbf{L}}_Z = \mathbf{L}_{ZZ} - \mathbf{L}_{ZL}\mathbf{L}_{LL}^{-1}\mathbf{L}_{LZ}, \tag{A22}$$

$$\bar{\mathbf{L}}_L(\omega) = \mathbf{L}_{LL} - \mathbf{L}_{LZ}\mathbf{L}_{ZZ}(\omega)^{-1}\mathbf{L}_{ZL}, \tag{A23}$$

$$\mathbf{L}_{ZL} = \mathbf{F}_{KZ}^T\tilde{\mathbf{L}}_K\bar{\mathbf{F}}_{KL}, \tag{A24}$$

$$\mathbf{L}_{LZ} = \mathbf{F}_{KL}^T\tilde{\mathbf{L}}_K\mathbf{F}_{KZ}, \tag{A25}$$

$$\mathbf{L}_{ZZ} = \mathbf{L}_Z + \mathbf{F}_{KZ}^T\tilde{\mathbf{L}}_K\mathbf{F}_{KZ}, \tag{A26}$$

$$\mathbf{L}_{LL} = \bar{\mathbf{L}} + \mathbf{F}_{KL}^T\tilde{\mathbf{L}}_K\bar{\mathbf{F}}_{KL}, \tag{A27}$$

$$\bar{\mathbf{F}}_{CY} = \mathbf{F}_{CY} + \mathbf{F}_{CL}\mathbf{L}^{-1}\mathbf{L}_{LK}\bar{\mathbf{L}}_K^{-1}\tilde{\mathbf{L}}_K\mathbf{F}_{KY}, \quad Y = Z,B, \tag{A28}$$

$$\bar{\mathbf{F}}_{KL} = \mathbf{F}_{KL} - \mathbf{L}_K^{-1}\mathbf{L}_{LK}^T, \tag{A29}$$

$$\tilde{\mathbf{L}}_L = \bar{\mathbf{L}}(\mathbf{1}_L + \mathbf{L}^{-1}\mathbf{L}_{LK}\bar{\mathbf{L}}_K^{-1}\tilde{\mathbf{L}}_K\bar{\mathbf{F}}_{KL})^{-1}, \tag{A30}$$

$$\tilde{\mathbf{L}}_K = \bar{\mathbf{L}}_K(\mathbf{1}_K - \mathbf{L}_K\bar{\mathbf{F}}_{KL}\mathbf{L}^{-1}\mathbf{L}_{LK}\bar{\mathbf{L}}_K^{-1})^{-1}, \tag{A31}$$

$$\bar{\mathbf{L}}_K = \mathbf{L}_K - \mathbf{L}_{LK}^T\mathbf{L}^{-1}\mathbf{L}_{LK}, \tag{A32}$$

$$\bar{\mathbf{L}} = \mathbf{L} - \mathbf{L}_{LK}\mathbf{L}_K^{-1}\mathbf{L}_{LK}^T. \tag{A33}$$

The last two terms of Eq. (A16) describe dissipation, handled by the Caldeira-Leggett formalism (see Ref. 8), to be reviewed momentarily. The remaining terms are generated by a (time dependent) system Hamiltonian:

$$\mathcal{H}_S(t) = \frac{1}{2}\mathbf{Q}_C^T\mathbf{C}^{-1}\mathbf{Q}_C + \left(\frac{\Phi_0}{2\pi}\right)U(\boldsymbol{\varphi},t), \tag{A34}$$

$$U(\varphi,t) = -\sum_i L_{J;i}^{-1}\cos\varphi_i + \frac{1}{2}\boldsymbol{\varphi}^T\mathbf{M}_0\boldsymbol{\varphi} + \frac{2\pi}{\Phi_0}\boldsymbol{\varphi}^T[(\bar{\mathbf{N}} * \mathbf{\Phi}_x)(t) + (\bar{\mathbf{S}} * \mathbf{I}_B)(t)]. \tag{A35}$$

Performing a standard Born-Markov approximation for the system dynamics, one obtains predictions for the relaxation times of the system

$$\frac{1}{T_1} = 4|\langle 0|\mathbf{m}\cdot\boldsymbol{\varphi}|1\rangle|^2 J(\omega_{01})\coth\frac{\omega_{01}}{2k_BT}, \tag{A36}$$

$$\frac{1}{T_\phi} = |\langle 0|\mathbf{m}\cdot\boldsymbol{\varphi}|0\rangle - \langle 1|\mathbf{m}\cdot\boldsymbol{\varphi}|1\rangle|^2 \left.\frac{J(\omega)}{\omega}\right|_{\omega\to 0} 2k_BT. \tag{A37}$$

We consider the external impedances contributing to decoherence one at a time (for an analysis of nonadditive effects, see Ref. 10). $\mathbf{M}_d(\omega)$, which determines the quantities in Eqs. (A36) and (A37), then has the form

$$\mathbf{M}_d(\omega) = \mu K(\omega)\mathbf{m}\mathbf{m}^T, \tag{A38}$$

$$K(\omega) = \bar{\mathbf{L}}_Z^{-1}(\omega), \tag{A39}$$

$$\mu = |\bar{\mathbf{m}}|^2, \tag{A40}$$

$$\mathbf{m} = \bar{\mathbf{m}}/\sqrt{\mu} = \bar{\mathbf{m}}/|\bar{\mathbf{m}}|, \tag{A41}$$

where $K(t)$ is a scalar real function, $\mathbf{m}$ is the normalized vector parallel to $\bar{\mathbf{m}}$, and $\sqrt{\mu}$ is the length of the vector $\bar{\mathbf{m}}$ (μ is the eigenvalue of the rank 1 matrix $\bar{\mathbf{m}}\bar{\mathbf{m}}^T$). Also

$$J(\omega) = -\mu\left(\frac{\Phi_0}{2\pi}\right)^2 \mathrm{Im}\, K(\omega). \tag{A42}$$

New results

The following expressions were not contained in BKD, and are new to this paper. The full frequency dependent expressions for $\bar{\mathbf{S}}$ and $\bar{\mathbf{N}}$ in Eq. (A16) are

$$\bar{\mathbf{S}}(\omega) = \bar{\mathbf{F}}_{CB} - \{\bar{\mathbf{F}}_{CZ}\bar{\mathbf{L}}_Z^{-1}(\omega)(\mathbf{F}_{KZ}^T - \mathbf{L}_{ZL}\mathbf{L}_{LL}^{-1}\mathbf{F}_{KL}^T) + \mathbf{F}_{CL}\tilde{\mathbf{L}}_L^{-1}\bar{\mathbf{L}}\bar{\mathbf{L}}_L^{-1}[\mathbf{F}_{KL}^T - \mathbf{L}_{LZ}\mathbf{L}_{ZZ}^{-1}(\omega)\mathbf{F}_{KZ}^T]\}\tilde{\mathbf{L}}_K\mathbf{F}_{KB}, \tag{A43}$$

$$\bar{\mathbf{N}}(\omega) = \mathbf{F}_{CL}\tilde{\mathbf{L}}_L^{-1}\mathbf{L}\mathbf{L}_L^{-1}(\omega) - \bar{\mathbf{F}}_{CZ}\bar{\mathbf{L}}_Z^{-1}(\omega)\mathbf{L}_{ZL}\mathbf{L}_{LL}^{-1}. \tag{A44}$$

In our previous work we assumed that $\mathbf{I}_B$ and Φ_x were time independent, so that only the $\omega\to 0$ limit of these expressions were presented.

A final result: it is amusing the write out the full expression for $\bar{\mathbf{N}}(\omega=0)$, from which $\mathbf{M}_0$ is easily constructed, in terms of the basic input matrices (loop matrices $\mathbf{F}$ and inductance matrices $\mathbf{L}$):

$$\bar{\mathbf{N}}(\omega=0)=\mathbf{F}_{CL}\{\mathbf{1}_L+\mathbf{L}^{-1}\mathbf{L}_{LK}(\mathbf{L}_K-\mathbf{L}_{LK}^T\mathbf{L}^{-1}\mathbf{L}_{LK})^{-1}[\mathbf{1}_K-\mathbf{L}_K(\mathbf{F}_{KL}-\mathbf{L}_K^{-1}\mathbf{L}_{LK}^T)\mathbf{L}^{-1}\mathbf{L}_{LK}(\mathbf{L}_K-\mathbf{L}_{LK}^T\mathbf{L}^{-1}\mathbf{L}_{LK})^{-1}]^{-1}\mathbf{L}_K(\mathbf{F}_{KL}-\mathbf{L}_K^{-1}\mathbf{L}_{LK}^T)\}$$
$$\times\{\mathbf{L}-\mathbf{L}_{LK}\mathbf{L}_K^{-1}\mathbf{L}_{LK}^T+\mathbf{F}_{KL}^T[\mathbf{1}_K-\mathbf{L}_K(\mathbf{F}_{KL}-\mathbf{L}_K^{-1}\mathbf{L}_{LK}^T)\mathbf{L}^{-1}\mathbf{L}_{LK}(\mathbf{L}_K-\mathbf{L}_{LK}^T\mathbf{L}^{-1}\mathbf{L}_{LK})^{-1}]^{-1}\mathbf{L}_K(\mathbf{F}_{KL}-\mathbf{L}_K^{-1}\mathbf{L}_{LK}^T)\}^{-1}. \quad \text{(A45)}$$

It is clear why it is more manageable to write this expression in terms of intermediate quantities; one can see that it involves up to four nested inverses.

[1] G. Burkard, D. P. DiVincenzo, P. Bertet, I. Chiorescu, and J. E. Mooij, Phys. Rev. B **71**, 134504 (2005).

[2] P. Bertet, I. Chiorescu, G. Burkard, K. Semba, C. J. P. M. Harmans, D. P. DiVincenzo, and J. E. Mooij, Phys. Rev. Lett. (to be published).

[3] Y. Nakamura, Yu. A. Pashkin, and J. S. Tsai, Nature (London) **398**, 786 (1999).

[4] Y. Makhlin, G. Schön, and A. Shnirman, Rev. Mod. Phys. **73**, 357 (2001).

[5] R. H. Koch, J. R. Rosen, G. A. Keefe, F. M. Milliken, C. C. Tsuei, J. R. Kirtley, and D. P. DiVincenzo, Phys. Rev. B **72**, 092512 (2005).

[6] R. H. Koch, G. A. Keefe, F. M. Milliken, J. R. Rosen, C. C. Tsuei, J. R. Kirtley, and D. P. DiVincenzo, Phys. Rev. Lett. **96**, 127001 (2006).

[7] G. Burkard, R. H. Koch, and D. P. DiVincenzo, Phys. Rev. B **69**, 064503 (2004).

[8] A. O. Caldeira and A. J. Leggett, Ann. Phys. (N.Y.) **149**, 374 (1983); Phys. Rev. A **31**, 1059 (1985).

[9] E. Mertzbacher, *Quantum Mechanics*, 2nd ed., (Wiley, New York, 1970).

[10] G. Burkard and F. Brito, Phys. Rev. B **72**, 054528 (2005).

[11] We choose the Fourier transform such that it yields the impedance $Z(\omega)=+i\omega L$ for an inductor (inductance L).